Luis A. Ferraz-Albani
Department of Mechanical Engineering,
University of Alberta,
Edmonton, AB T6G 2G8, Canada

Alberto Baldelli
Department of Mechanical Engineering,
University of Alberta,
Edmonton, AB T6G 2G8, Canada

Chrissy J. Knapp
Department of Chemistry,
University of Alberta,
Edmonton, AB T6G 2G2, Canada

Wolfgang Jäger
Department of Chemistry,
University of Alberta,
Edmonton, AB T6G 2G2, Canada

Reinhard Vehring
Department of Mechanical Engineering,
University of Alberta,
Edmonton, AB T6G 2G8, Canada

David S. Nobes
Department of Mechanical Engineering,
University of Alberta,
Edmonton, AB T6G 2G8, Canada

Jason S. Olfert[1]
Department of Mechanical Engineering,
University of Alberta,
Edmonton, AB T6G 2G8, Canada
e-mail: jolfert@ualberta.ca

Larry W. Kostiuk
Department of Mechanical Engineering,
University of Alberta,
Edmonton, AB T6G 2G8, Canada

Enhanced Evaporation of Microscale Droplets With an Infrared Laser

Enhancement of water droplet evaporation by added infrared radiation was modeled and studied experimentally in a vertical laminar flow channel. Experiments were conducted on droplets with nominal initial diameters of 50 μm in air with relative humidities ranging from 0% to 90% RH. A 2800 nm laser was used with radiant flux densities as high as $4 \times 10^5 W/m^2$. Droplet size as a function of time was measured by a shadowgraph technique. The model assumed quasi-steady behavior, a low Biot number liquid phase, and constant gas–vapor phase material properties, while the experimental results were required for model validation and calibration. For radiant flux densities less than $10^4 W/m^2$, droplet evaporation rates remained essentially constant over their full evaporation, but at rates up to 10% higher than for the no radiation case. At higher radiant flux density, the surface-area change with time became progressively more nonlinear, indicating that the radiation had diminished effects on evaporation as the size of the droplets decreased. The drying time for a 50 μm water droplet was an order of magnitude faster when comparing the $10^6 W/m^2$ case to the no radiation case. The model was used to estimate the droplet temperature. Between 10^4 and $5 \times 10^5 W/m^2$, the droplet temperature changed from being below to above the environment temperature. Thus, the direction of conduction between the droplet and the environment also changed. The proposed model was able to predict the changing evaporation rates for droplets exposed to radiation for ambient conditions varying from dry air to 90% relative humidity.
[DOI: 10.1115/1.4034486]

Keywords: droplet evaporation, infrared radiation, shadowgraph

1 Introduction

Droplet evaporation is of fundamental interest to a vast range of practical processes, which include topics as disparate as the combustion of liquid fuels in automotive engines and particle engineering in the pharmaceutical industry [1–3]. In most of these processes, a critical aspect is the rate of evaporation, which is the rate that liquid mass undergoes a phase change to its vapor state [4]. For example, hydrocarbon fuels react in their vapor state so the rate of their chemical enthalpy is converted to sensible energy, and subsequently the power of the system scales with the evaporation rate [5]. In particle engineering involving spray drying, the focus remains on the droplet and its increasing solute concentration as the solvent evaporates. The end state of the particle is highly dependent on the rate of evaporation and the dynamics of solute precipitation [4,6].

Fundamental understanding of the evaporation of an isolated droplet is well developed as a coupled heat and mass transfer problem, typically involving just the liquid and surrounding gas–vapor phases [7]. In that case, the liquid mass changes phase and diffuses away from the droplet to the surroundings. To balance the energy requirements for the phase change, heat by a series conduction–convection pathway flows inwards from the surroundings to the droplet. In terms of influencing or controlling the rate of evaporation, raising the thermal and chemical potential differences between the droplet and the surroundings (i.e., increasing the temperature and lowering the vapor concentration of the species that compose the liquid in the surroundings) increases the evaporation rate. Since there is a lower bound on this vapor concentration in the surroundings (i.e., zero relative humidity), the ability to increase the evaporation rate by this tactic is also limited. Such restrictions on the surrounding's temperature do not exist without consideration of other constraints, but overall the dynamic range in the rate of evaporation can be significant [8].

Alternatively, the evaporation rate can be affected by introducing a radiation component to supplement the conduction–convection heat transfer to the droplet. This method is widely appraised in the literature [3,9–17]. Elperin and Krasovitov [11] theoretically demonstrated the effect of radiation on the evaporation process. Subsequently, several studies focused their attention on the modeling of a droplet evaporation history influenced by a radiation source. The majority of the literature relies on a theoretical approach. For instance, Dombrovsky et al. [12] proposed a complex theoretical model with several limitations, including the

---

kind of solvents or radiation sources being considered. This model was then implemented on fuel droplets or the relationship between radiation power and droplet temperature [15]. Experimental approaches were recently used by Koh et al. [16] and Tatartchenko et al. [17], who both consider an aerosol subjected to laser radiation. However, the goals were to discover the transition phases of water [17] and the variation of radiation transmittance [16] and did not focus on the evaporation rate.

The literature lacks experimental work on the measurement of the enhancement of the evaporation rate of a droplet subjected to a radiation source. In addition, the observed results from the previous experimental work were not well supported by a model. Hence, the objectives of this paper are to contribute to both the experimental and modeling aspects of the evaporation rate of isolated droplets exposed to a constant radiation flux density. To achieve these objectives, the current work used a piezoceramic dispenser to inject water droplets in an environmentally controlled flow channel that transported the droplet along a path aligned to an infrared laser while using a shadowgraph technique to track the rate of change of the droplet diameter.

2 Experimental Setup and Methodology

The approach taken here to observe the evaporation of liquid water droplets was based on introducing isolated droplets produced by a piezoelectric generator into a transparent vertical airflow channel. This channel had well-controlled environmental conditions of temperature and relative humidity. The setup allowed the droplets to be exposed to infrared radiation and their diameters to be optically measured by shadowgraphy as a function of time. A schematic overview of the optomechanical experimental setup and the measurement system is shown in Fig. 1.

Droplet Generation. The production of a monodisperse droplet chain is often achieved in one of three different ways: via a thermic disperser [18], a vibrating orifice [19], or a piezoceramic dispenser [20]. Piezoceramic dispensers were chosen because they have an appropriately low droplet production rate for the current experiment [21–25], as well as other relative advantages in the proposed circumstances. For instance, in thermic dispensers, bubbles created inside the dispenser affect the droplet injection, but this is not the case for piezoceramic dispensers. Furthermore, piezoceramic dispensers produce consecutive droplets with a spacing sufficiently large to avoid droplet agglomeration faced in vibrating orifices [25].

All droplets studied were formed from distilled de-ionized water (#38796, Sigma-Aldrich Co. LLC., St Louis, MO) using a monodisperse droplet chain setup similar to the one described by Baldelli et al. [26]. The droplet generator consisted of a glass capillary tube with an orifice diameter of 30 μm surrounded by a piezoceramic element (MJ-AL-01-030, Microfab Technologies Inc., Plano, CA). The electrical signal used to actuate and trigger the piezoceramic component was a square-wave signal produced by a function generator (Model MD-E-3000, Microdrop Technologies GmbH, Mühlenweg, Norderstedt, Germany). The signal voltage amplitude and pulse width affected the initial droplet diameter, while the frequency altered the number of droplets per second. The amplitude was set so that the initial diameters were in the range of 47–50 μm. Measurements showed a Gaussian droplet diameter distribution with a standard deviation of the order of
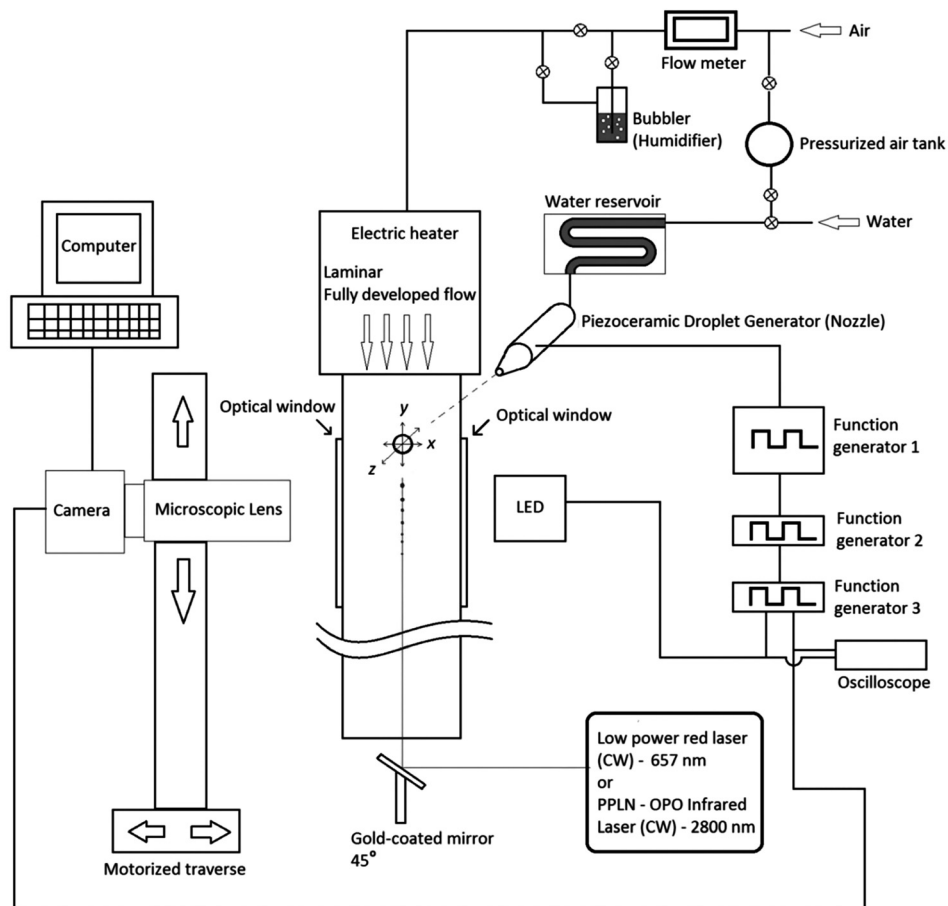

Fig. 1 Schematic of the experimental setup

1 μm. The production frequency was set to 1 Hz, so that the droplets could be considered isolated from each other. The droplet generator device was inserted into the port of the flow channel such that the device axis was oriented perpendicularly with respect to the flow tube axis, and the droplets projected into the flow tube such that they descended nominally along the tube's axis. A dual axis goniometer stage (Model GN2, Thorlabs Inc., Newton, NJ) and a single-axis translation stage (model PT1, Thorlabs Inc., Newton, NJ) were used to vary the position of the tip of the droplet generator in the x, y, and z directions, respectively. The liquid was fed into the droplet generator device by filling an S-shaped glass reservoir with a total volume of 2 ml using a polyethylene syringe (14-817-30, AirTite Norm-Jet Eccentric Luer Fisher Scientific, Edmonton, AB, Canada). Prior to filling the reservoir, the liquid was filtered through two 0.2 μm polytetrafluoroethylene (PTFE) filters (09-754-28, Corning PTFE 0.2 μm, Fisher Scientific, Edmonton, AB, Canada). Air from a pressurized tank assisted in the start-up of the droplet generator.

Airflow Channel. The vertical airflow channel was a cylindrical borosilicate glass tube with an internal diameter of 35 mm and a height of 400 mm, which was fed from its top aperture with a stream of air subsequently discharged at its bottom. A 6.5 mm diameter access port for the piezoelectric droplet generator was milled into the tube 50 mm from the top. This tube was further modified by milling out portions of the walls and replacing them with two flat optical-grade glass windows, 10 mm wide and 100 mm long. These windows were aligned to the tube's axis and opposite each other with their upper edges 35 mm from the top of the channel. These windows were adhered and sealed to the tube to allow the visualization of the droplets without distortion caused by observing the droplets through curved glass.

Air Supply. The airflow supplied to the vertical channel originated from a laboratory compressed air system. Its total volumetric flow rate was controlled manually by a set of precision needle valves (B-1KS4, Swagelok Inc., Edmonton Valve & Fitting, Edmonton, AB, Canada) and measured by a digital flow meter (4000 Series, TSI Inc., Shoreview, MN). A bypass system was implemented to send variable portions of dry air through a custom-built bubbler to control the relative humidity of the air when the streams were recombined. The bubbler consisted of a sealed glass container with two stainless steel tubes: the input tube was submerged in distilled de-ionized water (#38796, Sigma-Aldrich Co. LLC., St Louis, MO), and the output tube above the water level collected the humid air. Depending on the valve settings, relative humidities up to 90% at room temperature were obtainable. This humidified air was then passed through an electric heater located above the flow channel to achieve the various flow gas temperatures required for the different experiments. The air temperature was controlled (RK-89000-10, Digi-Sense, Cole Palmer, Laval, QC, Canada) using the output of a type-K thermocouple (TFE-K-20, Omega Engineering, Laval, QC, Canada) located at the same level as the droplet generator tip. The relative humidity of the airflow was measured by locating the probe of a digital hygrometer (Humicap HM70, Vaisala Inc., Richmond, BC, Canada) in the bottom of the flow channel. Once steady-state steady-flow conditions were achieved, the measured relative humidity had an uncertainty of $\pm 2\%$. While the airflow's temperature and relative humidity was variable, the flow rate of air was held at 1.0 slpm (± 0.1 slpm) to provide a near constant-velocity (flow velocity and settling velocity) moving frame of reference to transport the droplets. This flow rate was chosen to ensure laminar flow in the channel (Reynolds number based on the channel diameter, $\mathrm{Re}_C = 40$) and to avoid shedding from the droplet generator, which would create a von Karman vortex sheet. For the Reynolds number based on the generator diameter, i.e., 4, no shedding is expected [27]. Based on the energy and mass transfer Graetz numbers ($\mathrm{Gz}_T^{-1} = (L/D)/\mathrm{Re}\,\mathrm{Pr}$ and $\mathrm{Gz}_M^{-1} = (L/D)/\mathrm{Re}\,\mathrm{Sc}$,

respectively, where L is the channel length where the measurements were made, D is the channel diameter, Pr is the Prandtl Number, and Sc is the Schmidt Number) for these flows, and the length of the flow channel, the flow was within the entry-length ($\mathrm{Gz}_T^{-1} \sim \mathrm{Gz}_M^{-1} < 0.05$) [28]. Therefore, the inlet conditions of the channel remained constant along the channel's centerline over its whole length, even though the ambient temperature was different.

Infrared Radiation Source. Since water absorbs strongly in the short-wavelength infrared region, heating was expected at the moderate radiation flux density provided by an unfocussed infrared laser. Using a laser results in a low angle of divergence for easy manageability and safety [29], as well as maintaining a nearly constant radiation flux density along the droplet path.

The infrared radiation source was a periodically poled lithium niobate optical parametric oscillator, continuous wave laser (Aculight Argos SF-15, Lockheed Martin, Bothell, WA) tuned to a wavelength of 2799.8 $\pm$ 0.1 nm. The laser beam was reflected vertically upwards into the flow channel by a gold coated mirror (model NB1-L01, Thorlabs Inc., Newton, NJ), selected for its ~95% reflectance at the laser wavelength. An output power of 2.5 W at 2800 nm was obtained. To align the invisible beam, another continuous wave diode laser beam (model SNF Lasiris, Coherent Inc., Wilsonville, OR) with a wavelength of 657 nm was passed through the same optical system. The infrared laser was aligned coaxially with the vertical airflow channel to irradiate the droplets over their descent.

Experiments to determine the radiant flux density of the laser beam were performed. It was observed that the beam power density distribution was Gaussian. Based on two different definitions for the laser beam diameter, $1/e^2$ and the full width at half maximum, the calculated values of the beam diameters were approximately 3.9 mm and 2.6 mm, respectively, with a maximum local radiant flux density was estimated to be $4 \times 10^5\,\mathrm{W/m}^2$ when the total laser power was 2.33 W. The position of the droplet trajectory with respect to the laser beam cross-sectional could not be accurately determined; however, it was assumed to be invariant, since the setup remained unchanged during all the experiments and the experiments were repeatable.

Measuring Droplet Diameter. Once the droplets are produced and irradiated, one of the main requirements is the assessment of their diameter in order to estimate their evaporation rate. The method of shadowgraphy as an image-based technique for measuring particle size and shape has been used for different spray applications [30–33] and gas bubbles in effervescent atomization [34]. This technique allows for nonintrusive acquisition of images creating a shadow pattern that coincides with the projected shape and size of the measured object and is relatively simple. However, limitations exist for shadowgraphy for particle sizes below certain limits due to uncertainties associated with the image discretization by the pixels of the sensor [33] and indistinct boundaries [35]. To minimize these uncertainties, a minimum number of 40–50 pixels across the object was proposed by Podczeck et al. [35] and Ghaemi et al. [33].

The droplet diameter as a function of time was measured with a shadowgraphy technique using a microscope lens–CCD camera with a timed, stroboscopic back-illumination provided by a monochromatic light-emitting diode (LED) (mounted high power LEDs M530L3, Thorlabs, Newton, NJ), with a wavelength of 530 nm. A CCD camera (BM-500 GE GigE Vision, Pleora Technologies, Kanata, ON, Canada) was used to record the images. The 17 mm CCD sensor had a resolution of 2456 (horizontal) by 2058 (vertical) pixels. In trigger mode, the variable exposure time ranged from 64 μs to 2 s. Images collected by the camera were transferred to a computer for postprocessing. The microscope lens attached to the sensor (1-60068, 12$\times$ zoom system, Navitar, Rochester, NY) was operated at a zoom of 6$\times$ as a compromise between resolution and collection of light. For calibration, a multifunction, high

magnification calibration target (#56-076, Edmund Optics Inc., Nether Poppleton, York, UK) was used. This target was a 2.55 mm square grid composed of equally spaced vertical and horizontal lines (50 μm space between the lines and 2.5 μm line width) with an overall accuracy of $\pm 1\,\mu$m.

To capture images of the droplets in high resolution at various times, the entire camera, lens, and LED were mounted on a motorized computer-controlled vertical traverse (VXM-2 stepping motor controller, Velmex, Bloomfield, NY). The minimum displacement of the stepping motor was 6.35 μm per step. The camera was adjusted manually in x and z directions. The image collected by the sensor consisted of a bright field of view with the exception of the area where the droplets were located, in which shadows were recorded. Once located, at least 100 images were evaluated at each camera position in the flow tube to obtain the average droplet diameter with an acceptable uncertainty.

The algorithm for processing droplet images consisted of three steps. The first step consisted of the withdrawal of unfocused or unclear images. An image was saved only if it contained a drop in the center, with sharp contours and bright colors. The second and third steps were performed automatically in software (DAVIS 8.1.4, LaVision GmbH, Ypsilanti, MI) after selecting the proper particle recognition and sizing parameters. In the second step, the software recognized all the adjacent pixels that had intensities higher than the threshold, which was selected by the user. In the present work, several particle recognition intensity levels were tested, and the optimum value, which recognized the largest amount of particles, was selected. The third step consisted of measuring the diameter of the recognized particles by counting the total number of pixels and transforming the pixel area into physical area by using a calibration correlation.

The sensitivity to the selected threshold was also tested for a single experimental condition of 0% relative humidity and droplet lifetime of 0.42 s. It was observed that the size distributions of the droplet diameters were Gaussian for all chosen thresholds. Based on 100 images for each threshold, the values of the measured mean diameter ranged from 30.1 μm to 30.4 μm, and the standard deviations ranged from 0.7 μm to 0.8 μm. Hence, there was little variance of the mean diameter with respect to the varying threshold parameters. It was also observed that the difference between the maximum and minimum mean diameters was less than the minimum standard deviation. Including both precision and bias error, the total uncertainty in the droplet diameter was estimated to be $\pm 0.6\,\mu$m (95% confidence interval).

3 Numerical Model

Exposing an evaporating droplet to incident radiation disrupts the normal coupling between the basic physical processes of conduction heat transfer and mass diffusion as a droplet evaporates. For quasi-steady models of low Biot number droplets (i.e., uniform droplet temperature), the heat transfer from the surroundings to the droplet provides the energy needed to change the mass phase from liquid to vapor. As a result, with no incident radiation, the mass transfer rate of vapor from the droplet to the environment leads to the classic d-squared result [10,36–39]. This result was expected because all the key processes are surface-area-based phenomena, but the addition of nonisentropic thermal radiation to the droplet changes these relationships. The amount of radiation that intersects the droplet from a laser source also scales with d-squared, but the amount of energy absorbed will scale with the path length across the droplet (i.e., the diameter), so the d-squared relation would no longer be expected to apply.

Model Description. The model adopted here is of a stationary, quasi-steady, spherical, uniform liquid temperature, single-component, water droplet with its surface located at radius, r_s. This droplet is located in a quiescent environment of an inert gas (air) with far field boundary conditions of temperature, T_∞, and water vapor mass fraction, $Y_{w,\infty}$. The droplet is exposed to a

uniform radiant flux, $\dot{Q}''_{\mathrm{rad}}$, from one direction, and the amount of energy absorbed by the droplet is proportional to its absorptivity and the mean path length through the droplet for a total rate of radiation heat transfer, $\dot{Q}_{\mathrm{rad}}(r_s)$. In the steady-state limit, a unique thermal–compositional structure and rates of energy and mass transfer exist such that:

- the temperature of the liquid droplet and the gas–vapor mixture at the interface is $T_s(r_s)$.
- the mass fraction of water vapor immediately next to the droplet is in a saturated state, $Y_{w,s}(T_s)$.
- the mass flow rate of water vapor away from the droplet, $\dot{m}_w$, has an implied functional dependency of r_s and T_s.
- the temperature gradient in the gas–vapor mixture at the droplet interface is of a magnitude such that when the convection heat transfer is added to $\dot{Q}_{\mathrm{rad}}(r_s)$, there is sufficient total heat transfer to support the phase change of $\dot{m}_w$.
- the mass fraction gradient in the gas–vapor mixture at the droplet interface is of a magnitude such that when the diffusion mass transfer is added to any Stefan flow, the total sums to $\dot{m}_w$.

For a specified initial droplet size, $r_{s,0}$, and $\dot{Q}''_{\mathrm{rad}}$, the goal of the model is to predict T_s and $\dot{m}_w$ that can then be used to estimate the instantaneous time rate of change of r_s and then step forward in time through the evaporation process.

Droplet Conservation of Mass. The implication in the steady-state conservation of mass of a control volume that includes only the liquid droplet is that any mass evaporating from the surface of the droplet mass must be replaced by a mass source to the droplet

$$\dot{m}_{lw} = \dot{m}_{vw} = \dot{m}_w \tag{1}$$

where the subscripts "l," "v," and "w" stand for liquid, vapor, and water, respectively. The model adopted for the mass source is that it is at the same temperature as the liquid in the droplet and that there is no enthalpy transport into the droplet by the liquid.

Droplet Conservation of Energy. Applying the conservation of energy to a control volume that includes only the liquid droplet results in the following equation:

$$\dot{m}_w = \frac{\left(\lambda_{gv}\,A_s\frac{dT}{dr}\Big|_{r=r_s}\right)_{gv} + \dot{Q}_{\mathrm{rad}}}{h_{lv}(T_s)} \tag{2}$$

where λ_{gv}, A_s, and $h_{lv}(T_s)$ are thermal conductivity, area of the droplet surface, and enthalpy of evaporation of water at T_s, respectively, and the subscript "gv" represents the gas–vapor phase. This expression provides one coupling between the phases and between heat and mass transfer occurring at the interface. The unknowns, i.e., the evaporation rate, temperature gradient in the gas–vapor phase, and the droplet temperature, are derived from three conservation equations applied to the region outside of the liquid droplet.

Gas–Vapor Conservation of Energy. Using the assumptions of ideal gas behavior and that the materials' properties are independent of r, which implies specific heat capacitance, C_p, and thermal conductivity are independent of gas–vapor mixture (given the subscripts gv) composition and temperatures, the differential form of the conservation energy, shown in Eq. (3), was derived.

$$\mathrm{Pe_T}\,\frac{dT}{dr} = \frac{1}{r}\frac{d}{dr}\left(r^2\,\frac{dT}{dr}\right) \tag{3}$$

Here, $\mathrm{Pe_T}$ is the local thermal Peclet number, given by the following equation:

$$\mathrm{Pe_T} = \frac{\dot{m}_\mathrm{w} C_{p,\mathrm{gv}}}{4\pi\lambda_\mathrm{gv} r} \qquad (4)$$

It is worth emphasizing that Eqs. (3) and (4) are expressions based on the conduction being the only mode of heat transfer in the gas–vapor phase, even though the droplet is moving relative to the flow in the channel. This relative motion introduces the possible need to consider forced convection, but previous experimental results from this same experimental setup without imposed radiation were successfully modeled without convection [38]. Furthermore, it is noted that maximum Reynolds number for the droplet sizes tested was 0.27 such that the biased error in heat transfer would be ~4% relative to conduction only if the spherical droplet was not expelling mass due to evaporation [40]. In general, the affect on heat and mass transfer of having mass being expelled from the sphere is complex, but for the relevant case of the ratio of the expelling velocity to the diffusional velocity less than unity [41] (and deploying the Colburn analogy [28] between drag forces and heat transfer) the overall impact would be negligible.

Equation (3) was integrated to give the result of

$$T(r) = T_\infty + (T_\mathrm{s} - T_\infty) \frac{\exp(\mathrm{Pe_T}|_\mathrm{s})}{\exp(\mathrm{Pe_T})} \left[\frac{\exp(\mathrm{Pe_T}) - 1}{\exp(\mathrm{Pe_T}|_\mathrm{s}) - 1} \right] \qquad (5)$$

where $\mathrm{Pe_T}|_\mathrm{s}$ is the Peclet number evaluated at r_s. The justification for assuming constant specific heat capacity and thermal conductivity was considered reasonable for droplet temperatures that range from 2 °C to 42 °C for a water–air mixture with compositions ranging from dry to saturated air. In this domain of temperature and potential mass fractions of water, the ratio of $C_{p,\mathrm{gv}}/\lambda_\mathrm{gv}$ changes by less than 5% from the average of these extremes.

Equation (5) can be differentiated and substituted in Eq. (3), but there still remain one too many unknowns. Information regarding the equilibrium mass fraction of water vapor next to the droplet and the transport of mass by diffusion has yet to be imposed on the problem.

Vapor Conservation of Water Mass. Using the same set of assumptions as above, but also assuming that the diffusivity of water ($D_\mathrm{w,mix}$) is also a constant within Fick's Law, the differential equation for the transport of water in the gas–vapor phase becomes

$$\rho_\mathrm{gv} \mathrm{Pe_M} \frac{dY_\mathrm{w}}{dr} = \frac{1}{r} \frac{d}{dr}\left(r^2 \rho_\mathrm{gv} \frac{dY_\mathrm{w}}{dr} \right) \qquad (6)$$

where the local mass Peclet number is

$$\mathrm{Pe_M} = \frac{\dot{m}_\mathrm{w}}{4\pi\rho_\mathrm{gv} D_\mathrm{w,mix} r} \qquad (7)$$

Similar to the reasons presented for the energy equation, mass transfer is modeled only with diffusion and not including convection. Unlike the energy equation, Eq. (6) cannot be solved analytically due to the direct coupling of the density field to the temperature field (Eq. (5)) through ideal gas behavior, which can be made more explicit by substituting in the ideal gas law

$$\frac{\dot{m}_\mathrm{w} R}{4\pi P D_\mathrm{w,mix}} \frac{dY_\mathrm{w}}{dr} = \frac{d}{dr}\left(r^2 \frac{[Y_\mathrm{w} M_\mathrm{w} + (1 - Y_\mathrm{w})M_\mathrm{air}]}{T} \frac{dY_\mathrm{w}}{dr} \right) \qquad (8)$$

where M_w is the molecular mass of water, R is the universal gas constant, and P is pressure.

Solving for Evaporation Rate and Droplet Temperature. The system of equations above (Eqs. (2), (5), and (8)) needs to be solved with respect to boundary conditions. The challenge is that the temperature and water vapor mass fraction at r_s, though coupled through the equilibrium between the phases, are part of the solution. The other unknown is the water mass rate, $\dot{m}_\mathrm{w}$. The technique used to solve these equations was to identify the one-way coupling, in that the temperature field affects the solution of the mass fraction of water vapor field, but not vice versa. Therefore, Eqs. (2) and (5) can be solved for a specified T_s, $\dot{Q}''_\mathrm{rad}$, and r_s. That is, for each specified T_s, there is a corresponding $\dot{m}_\mathrm{w}$, such that without including Eq. (8) the solution is a function (i.e., not a unique solution) with $d\dot{m}_\mathrm{w}/dT_\mathrm{s}$ being negative. $T(r)$ can be included in the solution of Eqs. (2) and (5) for any specified T_s, which becomes an input to solve Eq. (8) for $Y_\mathrm{w,s}(r)$. Then, Eq. (8) can be solved for the corresponding $\dot{m}_\mathrm{w}$, which results in another solution function, but with $d\dot{m}_\mathrm{w}/dT_\mathrm{s}$ being positive. The intersection of these two functions corresponds to the only set of the boundary conditions and evaporation rate that are consistent with all the conservation equations for a given set of r_s, $\dot{Q}''_\mathrm{rad}$, T_∞, and $Y_\mathrm{w,\infty}$. All material properties were calculated as described in the standard model [38,41]. $Y_\mathrm{w,s}(T_\mathrm{s})$ was calculated using an Antoine equation [42].

Evaporation Rate Model Validation. The above evaporation model that includes radiation heat transfer was validated against experiments and the analytical model of Vehring et al. [38] for the case of no radiation. It can be observed in Fig. 2, that in the case of lower air temperature, i.e., $T_\infty = 19.8$ °C, a reduction in the average diameter from 46.5 μm to 37.7 μm occurred in the 0.5 s that the droplets were visible in the measurement windows. This represents a reduction in diameter, surface area, and volume of approximately 19%, 34%, and 47%, respectively, from its initial values. When the temperature of the surrounding air was 60 °C, the droplet diameter decreased from 49.1 μm to 29.5 μm in the 0.4 s available to observe those droplets. The time to observe the droplets at higher temperatures was shorter because the airflows were both controlled to be 1 slpm, which means the actual volume flow rate was higher for the higher temperature case. This change in size represents a reduction of the diameter, surface area, and volume of approximately 40%, 64%, and 78%, respectively. In the figure, the experimental data points are generally lower than the current model, although most points are within the two standard deviation band of the initial droplet diameter. The current model and the analytical model of Vehring et al. [38] agree well and produce almost identical results for the low temperature case (the lines overlap). Hence, the model was successfully validated for the case without radiation.

4 Results and Discussions: Experiments and Model

Table 1 shows the experimental conditions tested with radiation heat transfer from the laser. Comparison of experimental data (known total powers and spatial distribution of that power) to
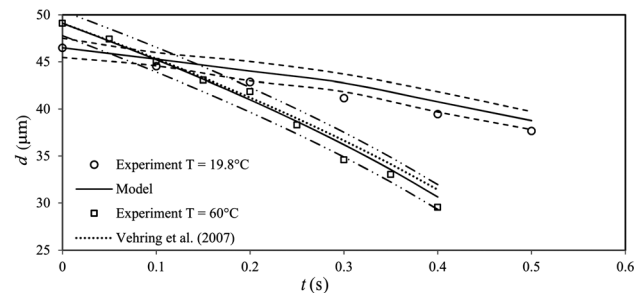
Fig. 2 Comparison between the experimental and model results for different conditions of air temperature ($T_\infty = 19.8$ °C and $T_\infty = 60$ °C) and 0% relative humidity. Dashed lines represent a two standard deviation band in the measured initial diameters.

Table 1 Experimental test conditions, i.e., ambient temperature, ambient relative humidity, initial droplet diameter ($d_s, 0$), and the standard deviation in the initial diameter ($S_{d,0}$). Due to difficulties in precisely setting the laser power, it was necessary to measure that quantity for each case.

Case #	T_∞ (°C)	RH_∞ (%)	$d_{s,0}$ (μm)	$S_{d,0}$ (μm)	Total laser power (W)
1	20.0	0	50	1.1	2.33
2	24.0	0	48	0.8	2.33
3	24.6	30	50	0.8	2.33
4	23.7	60	48	0.7	1.91
5	24.3	90	48	0.7	2.37

numerical results (based on total rate of radiation heat transfer to the droplet as a function of its diameter) required a calibration between radiant flux density and radiation heat transfer.

Converting Radiant Flux Density to Radiation Heat Transfer. The experiments were based on exposing the droplet to a unidirectional radiation field with uniform radiant flux density, while Eq. (2) of the model is based on the radiation heat flux added to the liquid. There are many factors that can affect converting radiant flux to energy transferred to the droplet, including the droplet diameter, wavelength of the laser, and the absorptive, reflective, transmissive, and scattering properties of the water and its interface at that wavelength.

Since all the cases tested used the same laser and physical layout, this complex conversion can be reduced to a calibration process by using one set of experimental data. Case #1 was used to calibrate the model for comparison to all the other experimental data collected. Figure 3 shows how the d-squared changes in time for radiation flux densities varying from 0 to 1×10^7 W/m². Using the experimental data for case #1 between the 2×10^5 and 5×10^5 W/m² flux densities, and based on a least squares fit, it was determined that the model was most consistent with a radiation flux density that was 55% of the peak radiation flux density when the total laser power was 2.33 W. Therefore, in all other model results, the incident radiation flux density was set to be 55% of the peak expected from the measured total power for those experiments due to the droplet not being aligned with the maximum radiation flux density.

Droplet Diameter as a Function of Time. Figure 3 shows some basic features of how the incident radiation affects the change in droplet diameter with time. For radiation flux densities of 1×10^4 W/m² (i.e., ten times the terrestrial radiant flux density of the sun, but now in a single highly absorptive wavelength) and less, there was only a modest effect on the evaporation rate. The total time to evaporate a droplet exposed to 1×10^4 W/m² was only 10% shorter than for the same droplet (48.12 μm) and environmental conditions (RH = 0%, $T_\infty = 20$ °C) with no incident

radiation. Given the low relative humidity, this may not be unexpected and reaffirms that the driving mechanism for evaporation is the gradient in water vapor mass fraction.

Figure 3 highlights that when the incident radiation was 2×10^5 W/m² or greater the slope of d-squared with respect to time is no longer constant. This result indicates that the incident radiation becomes less effective in supporting evaporation as the droplet becomes smaller. While the area of intercepted radiation effectively scales with surface area, which also scales with d-squared, the droplet's depth also becomes smaller, and a reduced portion of incident radiation is absorbed. Since the instantaneous rate of diameter or d-squared changes over the evaporation process, it is easier to compare the total time needed to evaporate a droplet. The case of 10^6 W/m² has a total evaporation time that is an order of magnitude shorter than the no radiation case.

Droplet Temperature During Evaporation. The temperature of the droplet as a function of time and incident radiation flux density was not available experimentally, but this information was part of the model's solution. Figure 4 shows how the droplet temperature changes as a function of diameter, normalized by the initial droplet diameter. For this figure, the droplet evolution is right-to-left. For the cases of no incident radiation and 1×10^4 W/m², the droplet temperature was essentially constant and 15 K lower than the ambient air temperature, which set the direction of heat transfer to be from the environment to the droplet. For the highest case shown, 1×10^6 W/m², the droplet temperature was predicted to be over 40 K above the ambient air temperature near its initial state, which means that the direction of conduction heat transfer is reversed. As the droplet is affected by the incident radiation, it becomes smaller and its temperature decreases, which is further indication that heat transfer by radiation is becoming less effective in providing energy to aid in evaporation. Tracking the droplet temperature in the model is also important in determining if some of the modeling assumptions have been violated. In particular, as the temperature of the droplet rises above 315 K (42 °C), the assumption of spatially uniform material properties reaches ±5% limit, and greater care needs to be taken in interpreting the results quantitatively.

Comparing Experimental Results to Numerical Model. Figure 5 shows the measured and modeled results for cases #2–5 using the single calibration derived from the results of case #1. Each of these figures includes the experimental data of mean droplet diameter at different times, model results for the calibrated radiant flux density for the mean initial diameter (solid line) and initial diameters two standard deviations larger and smaller (dashed lines), and model results if there were no incident radiation (dashed-dotted lines). Few of the data points fell outside the bounds of variation in initial droplet size (two standard deviations), and those incidences were concentrated in the 90% ambient relative humidity case. As a result, this simple model appears to have captured the key aspects of the evaporation processes with incident radiation without the inclusion of convection.
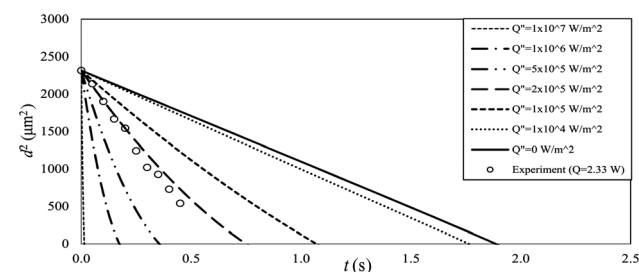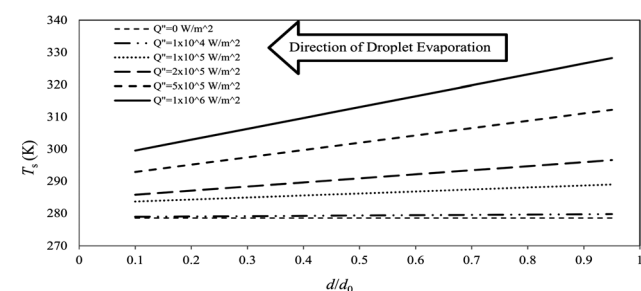
Fig. 3 Evolution of squared diameter (micrometers squared) with respect to time (seconds) for pure water droplets with conditions of RH = 0%, T_∞ = 20 °C, initial diameter of 48.12 μm, and varying infrared radiation

Fig. 4 Variation of the surface temperature of water droplets, T_s, with respect to droplet diameter for various infrared radiant flux densities, RH = 0%, and T_∞ = 293.15 K
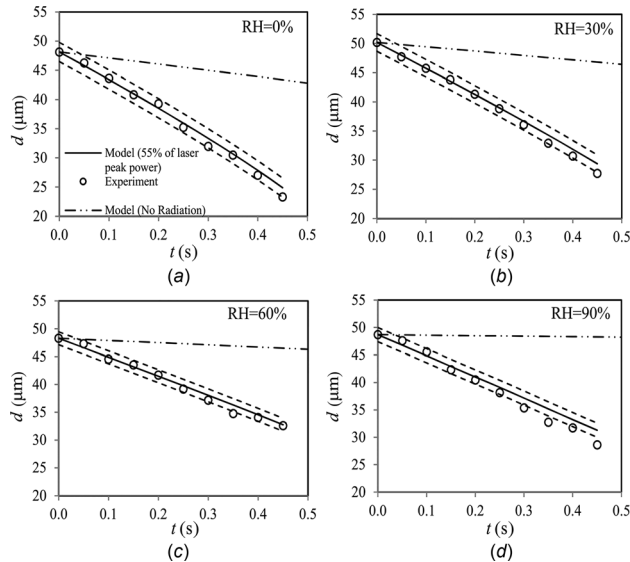
Fig. 5 Comparison between the experimental and numerical model results for water droplets subject to infrared radiation and different conditions of relative humidity. Dashed lines represent two standard deviations in the initial droplet diameter. (a) $T_\infty = 24.0\,°C$, RH = 0%, power = 2.33 W, and standard deviation of initial droplet diameter ($S_{d,0}$) = 0.81 μm; (b) $T_\infty = 24.6\,°C$, RH = 30%, power = 2.33 W, and $S_{d,0}$ = 0.81 μm; (c) $T_\infty = 23.7\,°C$, RH = 60%, power = 1.91 W, and $S_{d,0}$ = 0.67 μm; and (d) $T_\infty = 24.3\,°C$, RH = 90%, power = 2.37 W, and $S_{d,0}$ = 0.65 μm.

In all cases, it was observed that the incident radiation had a significant influence on the rate of evaporation, with the largest difference occurring when the environment has the highest relative humidity. Without the incident radiation, the 90% relative humidity droplet would not expect to change diameter over the observed 0.45 s period, while with the exposure to radiation on it evaporated 75% of its mass.

5 Conclusions

This study considered an experimental and modeling approach for the purpose of investigating the enhancement of water droplet evaporation by infrared radiation. Experiments were conducted in a vertical flow channel on isolated droplets with initial diameters of ~50 μm in a stream of air with a specified temperature and relative humidity. A single wavelength (2.8 μm) infrared laser imposed constant radiation flux density on the droplet. The size of the droplets as a function of time was measured by a shadowgraph technique.

The model was based on a quasi-steady, spherically symmetric, low Biot number liquid phase, constant gas–vapor phase material properties' assumptions, and the unidirectional laser radiation. The conversion of incident radiation flux density to radiation heat transfer for the model was done by using one set of experimental results to calibrate the model.

Conclusions drawn from this study include:

(1) for incidence radiation flux densities of the order of 10^4 W/m^2 and less, the model predicts that the effects of the radiation on the evaporation rate are small. Plots of droplet diameter-squared with respect to time are essentially straight lines, and the slope varies by less than 10% from the no radiation case.

(2) at higher radiation flux densities, the relationship of diameter-squared with time is progressively nonlinear such that the incident radiation had a diminishing effect on the evaporation rate as the droplet diameter decreased. The total time to evaporate a 50 μm water droplet in dry air at 20 °C at a radiation flux density of 10^6 W/m^2 is predicted to

be an order of magnitude faster than the no radiation case. This effect can be considerably greater at higher ambient humidity due to the droplet temperature being above that of the surrounding gas–vapor phase.

(3) the model calculated the droplet temperature as a function of incident radiation flux density and droplet diameter for the ambient conditions of 20 °C and dry air. For the same lower range (i.e., <10^4 W/m^2) of radiation flux density, the droplet temperature is constant and subambient (essentially the wet bulb temperature) for droplet sizes of 50 μm and less. At higher flux densities, the droplet temperature is a function of droplet diameter, and above 5×10^5 W/m^2 the droplet temperature is above the gas temperature, so that the direction of heat transfer is opposite to the lower radiation situation.

(4) once calibrated with a single set of experiment results, the proposed simple model is able to predict the evaporation rates for 50 μm droplets exposed to high radiation flux densities for ambient conditions varying from dry air to that at 90% relative humidity.

Nomenclature

A = area (m^2)
C_p = specific heat capacity (J/kg K)
d = droplet diameter (m)
D = mass diffusion coefficient (m^2/s)
h = specific enthalpy (J/kg)
M = molecular mass (kg/kmol)
$\dot{m}$ = mass flux (kg/s)
P = pressure (kPa)
Pe_M = mass Peclet number
Pe_T = thermal Peclet number
Q = heat transfer per unit time (W/m^2)
$\dot{Q}''$ = heat transfer per unit time per unit area (W/m^2)
r = droplet radius (m)
R = universal gas constant (8.314 kJ/kmol K)
Re = Reynolds number
$S_{d,0}$ = standard deviation of initial droplet diameter
T = temperature (K, °C)
u = velocity (m/s)
Y = mass fraction (kg of k – species/kg of mixture)
λ = thermal conductivity (W/m K)
ρ = density (kg/m^3)

Subscripts

gv = gas–vapor phase
l = liquid
mix = mixture
rad = radiative, radiation
s = surface
v = vapor
w = water
0 = initial
∞ = infinity

References

[1] Ejima, H., Richardson, J. J., Liang, K., Best, J. P., van Koeverden, M. P., Such, G. K., Cui, J., and Caruso, F., 2013, "One-Step Assembly of Coordination Complexes for Versatile Film and Particle Engineering," Science, **341**(6142), pp. 154–157.
[2] Kitano, T., Nishio, J., Kurose, R., and Komori, S., 2014, "Evaporation and Combustion of Multicomponent Fuel Droplets," Fuel, **136**, pp. 219–225.

[3] McAllister, S., Chen, J.-Y., and Fernandez-Pello, A. C., 2011, "Droplet Evaporation and Combustion," *Fundamentals of Combustion Processes*, Springer, Berlin, pp. 155–175.

[4] Sharma, S., and Debenedetti, P. G., 2012, "Evaporation Rate of Water in Hydrophobic Confinement," Proc. Natl. Acad. Sci., **109**(12), pp. 4365–4370.

[5] Ranjbar, H., and Shahraki, B. H., 2013, "Effect of Aqueous Film-Forming Foams on the Evaporation Rate of Hydrocarbon Fuels," Chem. Eng. Technol., **36**(2), pp. 295–299.

[6] Chan, H.-K., and Kwok, P. C. L., 2011, "Production Methods for Nanodrug Particles Using the Bottom-Up Approach," Adv. Drug Delivery Rev., **63**(6), pp. 406–416.

[7] Vehring, R., 2008, "Pharmaceutical Particle Engineering Via Spray Drying," Pharm. Res., **25**(5), pp. 999–1022.

[8] Rogers, S., Fang, Y., Qi Lin, S. X., Selomulya, C., and Dong Chen, X., 2012, "A Monodisperse Spray Dryer for Milk Powder: Modelling the Formation of Insoluble Material," Chem. Eng. Sci., **71**, pp. 75–84.

[9] Twomey, S., 1991, "Aerosols, Clouds and Radiation," Atmos. Environ., Part A, **25**(11), pp. 2435–2442.

[10] Hara, H., and Kumagai, S., 1994, "The Effect of Initial Diameter on Free Droplet Combustion With Spherical Flame," Proc. Combust. Inst., **25**(1), pp. 423–430.

[11] Elperin, T., and Krasovitov, B., 1995, "Evaporation of Liquid Droplets Containing Small Solid Particles," Int. J. Heat Mass Transfer, **38**(12), pp. 2259–2267.

[12] Dombrovsky, L., Sazhin, S., Sazhina, E. M., Feng, G., Heikal, M. R., Bardsley, M., and Mikhalovsky, S., 2001, "Heating and Evaporation of Semi-Transparent Diesel Fuel Droplets in the Presence of Thermal Radiation," Fuel, **80**(11), pp. 1535–1544.

[13] Tseng, C., and Viskanta, R., 2005, "Effect of Radiation Absorption on Fuel Droplet Evaporation," Combust. Sci. Technol., **177**(8), pp. 1511–1542.

[14] Abramzon, B., and Sazhin, S., 2006, "Convective Vaporization of a Fuel Droplet With Thermal Radiation Absorption," Fuel, **85**(1), pp. 32–46.

[15] Sazhin, S. S., 2006, "Advanced Models of Fuel Droplet Heating and Evaporation," Prog. Energy Combust. Sci., **32**(2), pp. 162–214.

[16] Koh, H.-S., Shin, W.-S., Jeon, M.-Y., and Park, B.-S., 2012, "The Variation of Radiation Transmittance by the cw 1.07 μm Fiber Laser and Water Aerosol Interaction," J. Opt. Soc. Korea, **16**(3), pp. 191–195.

[17] Tatartchenko, V., Liu, Y., Chen, W., and Smirnov, P., 2012, "Infrared Characteristic Radiation of Water Condensation and Freezing in Connection With Atmospheric Phenomena; Part 3: Experimental Data," Earth-Sci. Rev., **114**(3–4), pp. 218–223.

[18] Sgro, A. E., Allen, P. B., and Chiu, D. T., 2007, "Thermoelectric Manipulation of Aqueous Droplets in Microfluidic Devices," Anal. Chem., **79**(13), pp. 4845–4851.

[19] Shemirani, F. M., Azhdarzadeh, M., Mohammad, T., Fong, J., Church, T. K., Lewis, D. A., Finlay, W. H., and Vehring, R., 2012, "A Continuous, Monodisperse Propellant Microdroplet Stream as a Model System for Laser Analysis of Mass Transfer in Metered Dose Inhaler Sprays," Respir. Drug Delivery, **3**, pp. 773–776.

[20] Ulmke, H., Wriedt, T., and Bauckhage, K., 2001, "Piezoelectric Droplet Generator for the Calibration of Particle-Sizing Instruments," Chem. Eng. Technol., **24**(3), pp. 265–268.

[21] Luo, W., and Deng, G., 2013, "Simulation Analysis of Jetting Dispenser Based on Two Piezoelectric Stacks," 14th International Conference on Electronic Packaging Technology, IEEE, Changsha, China, Aug. 11–14, pp. 738–741.

[22] Sun, J., Fuh, J., Thian, E., Hong, G., Wong, Y., Yang, R., and Tan, K., 2013, "Fabrication of Electronic Devices With Multi-Material Drop-On-Demand Dispensing System," Int. J. Comput. Integr. Manuf., **26**(10), pp. 897–906.

[23] Gu, Z., Deng, G., and Zhou, C., 2014, "Study on Temperature Field of Fluid Jet-Dispenser Based on Two Piezoelectric Stacks," Applications of Ferroelectrics (ISAF), Chengdu, China, IEEE, pp. 684–687.

[24] Saleki-Haselghoubi, N., Shervani-Tabar, M. T., Taeibi-Rahni, M., and Dadvand, A., 2014, "Numerical Study on the Oscillation of a Transient Bubble Near a Confined Free Surface for Droplet Generation," *Theoretical and Computational Fluid Dynamics*, Springer, Berlin, pp. 1–24.

[25] Wen, Y., Deng, G., and Zhou, C., 2014, "Simulation Analysis of Jet Dispenser Based on Piezoelectric Actuators," 15th International Conference on Electronic Packaging Technology, Chengdu, China, pp. 680–683.

[26] Baldelli, A., Boraey, M. A., Nobes, D., and Vehring, R., 2015, "Analysis of the Particle Formation Process of Structured Microparticles," Mol. Pharm., **12**(8), pp. 2562–2573.

[27] Tritton, D. J., 1959, "Experiments on the Flow Past a Circular Cylinder at Low Reynolds Numbers," J. Fluid Mech., **6**(4), pp. 547–567.

[28] Incorpera, F. P., Dewitt, D. P., Bergman, T. L., and Lavine, A. S., 2007, *Fundamental of Heat and Mass Transfer*, 6th ed., Wiley, New York, p. 512.

[29] Ponkham, K., Meeso, N., Soponronnarit, S., and Siriamornpun, S., 2012, "Modeling of Combined Far-Infrared Radiation and Air Drying of a Ring Shaped-Pineapple With/Without Shrinkage," Food Bioprod. Process., **90**(2), pp. 155–164.

[30] Simmons, H. C., 1977, "The Correlation of Droplet-Size Distibution in Fuel Nozzle Sprays, Part I: The Droplet-Size/Volume-Fraction Distribution," J. Eng. Power, Ser. A, **99**(3), pp. 309–319.

[31] Oberdier, L. M., 1984, "An Instrumentation System to Automize the Analysis of Fuel-Spray Images Using Computer Vision," *Liquid Particle Size Measurement Techniques*, (ASTM STP 848), J. M. Tishkoff, R. D. Ingebo, and J. B. Kennedy, eds., American Society for Testing and Materials, Philadelphia, PA.

[32] Weiss, B. A., Derov, P., DeBiase, D., and Simmons, H. C., 1984, "Fluid Particle Sizing Using a Fully Automated Optical Imaging System," Opt. Eng., **23**, pp. 561–566.

[33] Ghaemi, S., Rahimi, P., and Nobes, D., 2008, "Measurement of Droplet Centricity and Velocity in the Spray Field of an Effervescent Atomizer," ASME Paper No. FEDSM2008-55046, pp. 617–625.

[34] Gomez, J., Fleck, B., Olfert, J., and McMillan, J., 2011, "Influence of Two-Phase Feed Bubble Size on Effevescent Atomization in a Horizontal Nozzle Assembly," Atomization Sprays, **21**(3), pp. 249–261.

[35] Podczeck, F., Rahman, S., and Newton, J., 1999, "Evaluation of a Standardised Procedure to Assess the Shape of Pellets Using Image Analysis," Int. J. Pharm., **192**(2), pp. 123–138.

[36] Ali Al Zaitone, B., and Tropea, C., 2011, "Evaporation of Pure Liquid Droplets: Comparison of Droplet Evaporation in an Acoustic Field Versus Glass-Filament," Chem. Eng. Sci., **66**(17), pp. 3914–3921.

[37] Boraey, M. A., and Vehring, R., 2014, "Diffusion Controlled Formation of Microparticles," J. Aerosol Sci., **67**, pp. 131–143.

[38] Vehring, R., Foss, W. R., and Lechuga-Ballesteros, D., 2007, "Particle Formation in Spray Drying," J. Aerosol Sci., **38**(7), pp. 728–746.

[39] Vicente, J., Pinto, J., Menezes, J., and Gaspar, F., 2013, "Fundamental Analysis of Particle Formation in Spray Drying," Powder Technol., **247**, pp. 1–7.

[40] Dennis, S. C. R., Walker, J. D. A., and Hudson, J. D., 1973, "Heat Transfer From a Sphere at Low Reynolds Numbers," J. Fluid Mech., **60**(2), pp. 273–283.

[41] Rawls, W., Brakensiek, D., and Saxton, K., 1982, "Estimation of Soil Water properties," Trans. ASAE, **25**(5), pp. 1316–1320.

[42] Senol, A., 2013, "Solvation-Based Vapour Pressure Model for (Solvent + Salt) Systems in Conjunction With the Antoine Equation," J. Chem. Thermodyn., **67**, pp. 28–39.